Applied Mathematical Modelling 139 (2025) 115809

Contents lists available at ScienceDirect

Applied Mathematical Modelling

journal homepage: www.elsevier.com/locate/apm

An analytical 1D model for computing low-frequency electromagnetic fields in material layers: Application to metallurgical furnaces

Mads Fromreide [a,b,*], Dolores Gómez [b,c], Svenn Anton Halvorsen [a], Pilar Salgado [b,c]

[a] NORCE Norwegian Research Centre AS, Universitetsveien 19, 4630 Kristiansand, Norway
[b] Department of Applied Mathematics, Universidade de Santiago de Compostela, Santiago de Compostela, E-15782, Spain
[c] Galician Center for Mathematical Research and Technology (CITMAga), Santiago de Compostela, E-15782, Spain

ARTICLE INFO

Keywords:
Submerged arc furnaces
Induction
Proximity effect
Analytical 1D models
2D models

ABSTRACT

An analytical one-dimensional model for the distribution of electric fields within multiple material layers is developed and analyzed. The model originates from the study of large three-phase electric smelting furnaces for ferroalloys and is derived from the low-frequency time-harmonic Maxwell's equations. A solution is obtained for a general case with N layers of material with different electromagnetic properties. A practical demonstration of the utility of the model is given through an application to a multilayer configuration representing the lining and casing in a FeMn furnace, with validation against 2D simulations. In addition, for a specific two-layer scenario with a highly conductive material, an approximate solution for the adjacent layer is derived. This approximation allows the distribution of the adjacent layer to depend only on its individual properties, and shows that the dissipated power reaches a maximum value when the skin depth/thickness ratio is around one. Comparative analysis between the analytical model and 2D simulations shows good qualitative agreement.

List of symbols and corresponding units

$\mathbf{B}$	Magnetic induction	T
$\mathbf{E}$	Electric field	$\mathrm{V\,m^{-1}}$
E_0	Electric field value at surface	$\mathrm{V\,m^{-1}}$
f	AC frequency	Hz
$\mathbf{H}$	Magnetic field	$\mathrm{A\,m^{-1}}$
I_{tot}	Total cross-section current per unit length	$\mathrm{A\,m^{-1}}$
$\mathbf{J}$	Current density	$\mathrm{A\,m^{-2}}$
α	complex number 1+i	-
δ	Skin depth, $\delta = 1/\sqrt{\pi f \mu \sigma}$	m
μ_0	Magnetic permeability of vacuum	$\mathrm{H\,m^{-1}}$
μ_r	Relative permeability	-
μ	Material permeability, $\mu = \mu_r \mu_0$	$\mathrm{H\,m^{-1}}$
σ	Electric conductivity	$\mathrm{S\,m^{-1}}$
ω	Angular frequency, $\omega = 2\pi f$	$\mathrm{s^{-1}}$

* Corresponding author at: NORCE Norwegian Research Centre AS, Universitetsveien 19, 4630 Kristiansand, Norway.
E-mail address: mafr@norceresearch.no (M. Fromreide).

https://doi.org/10.1016/j.apm.2024.115809
Received 26 April 2024; Received in revised form 5 November 2024; Accepted 8 November 2024

Available online 14 November 2024

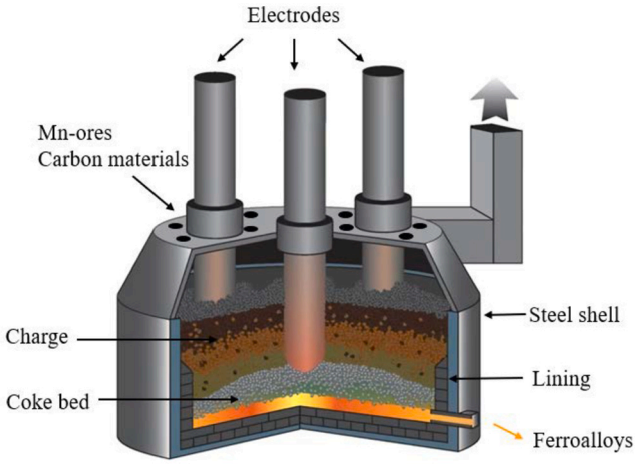

Fig. 1. Sketch of a submerged arc furnace for FeMn production (reproduced with permission from M. Tangstad).

1. Introduction

Ferroalloys, such as ferromanganese (FeMn) and ferrosilicon (FeSi), are produced by reducing oxide ores in large electric arc furnaces. These furnaces requires significant energy input, typically in excess of 40 megawatts, supplied as three-phase alternating current (AC) through electrodes immersed in the furnace hearth [1–3]. The energy provided by these currents, which typically reach about 100 kiloamperes, generates the heat necessary to drive a series of chemical reduction reactions that convert ores into metal and slag.

Fig. 1 shows the typical configuration of a submerged arc furnace (SAF) used for ferromanganese production, with three electrodes arranged in an equilateral triangle and submerged in the charge materials. These furnaces are typically over 10 meters in diameter, with electrode diameters ranging from 1 to 2 meters. The raw materials composing the charge are introduced into the furnace through feeders located at the top, while the resulting molten metal and slag are collected at the bottom. The central part of a SAF operates at extremely high temperatures, often ranging between 1500 and 2000 °C. A special lining is used to protect the furnace from these intense conditions and to prevent corrosion. The inner lining is made of carbon/graphite and extends from the bottom along the sides to a height above the normal slag level. Between this lining and the external steel shell, bricks are used to cover the entire inside of the shell, providing additional protection. The steel shell needs to be cooled to secure its structural integrity, typically by radiation and natural air convection, which can be enhanced by the use of fans, cooling fins or even water cooling.

SAFs are designed for continuous operation with a lifespan of about ten years [2], interrupted only for essential maintenance. At the end of their life, furnaces can be excavated to study their internal structure, providing valuable insights. Such studies have identified various reaction zones and layered formations in its upper part (cf. Fig. 1) due to the increase in temperature with depth [4–6]. FeMn furnaces are characterized by a coke-enriched region (known as the coke bed) around and below each electrode tip, where heat is generated by ohmic heating [1].

Due to the high temperatures and chemically hostile environment in the furnace hearth, direct measurements of the internal conditions are very difficult, if not impossible. Mathematical models and numerical simulations are therefore important tools to improve understanding and aiding in furnace design and efficient process control. A complete knowledge of the whole process requires a detailed study of a highly coupled physical phenomena including electromagnetics, heat transfer, fluid dynamics, structural mechanics and chemical reactions. In this paper we will focus only on the electromagnetics aspects, omitting the coupling with other physics.

The electromagnetic problem in three-phase furnaces has been extensively studied. In early works and in larger multiphysics models, the problem was often simplified by using direct current (DC) instead of AC (see, for instance, [7–9]). With today's technology, full-scale 3D models of three-phase AC furnaces can be solved with reasonable computational effort using commercial numerical solvers such as COMSOL or ANSYS (see e.g. [10–14]). However, considering the full electromagnetic problem for a three-phase AC furnace is not the subject of this paper. The primary goal of this work is to provide a computationally efficient 1D analysis tool that strikes a balance between simplicity and accuracy in capturing key electromagnetic phenomena in metallurgical furnaces. More precisely, we will investigate how inductive effects affect the distribution of current and power on different materials, with particular focus on the multilayered lining and steel shell surrounding the furnace. We aim to provide a tool that enables quick qualitative insights into the distribution of electric fields across multiple material layers, and serves as a foundation that can be further refined using more detailed 2D or 3D models if needed.

The distribution of electromagnetic fields within the furnace is strongly influenced by the different electrical conductivities of its constituent materials. These materials include very good conductors (metal, electrodes), moderate conductors (slag, coke bed), and very low conducting and insulating materials (charge and insulating lining), which may also have different magnetic properties. The conductivity of the charge layers is significantly lower than that of the coke beds, indicating that most of the current from the electrodes flows through the coke beds into the liquid alloy or directly through the beds between the electrodes. Induction also

plays an important role in the distribution of electromagnetic fields in the furnace. For example, the redistribution of currents in the electrodes due to skin and proximity effects is well known (see, for instance, [12,13,15] and references therein). In addition, large currents are also induced in the steel shell surrounding the furnace [10].

In [16], the authors introduced reduced in-plane 2D and 1D models aimed at clarifying the inductive effects between the different regions in the hearth of the furnace. They also compared the use of true AC models with DC approximations. Based on the non-dimensional approach, different regimes of electrical behaviour were defined. The 1D model was then solved for two material layers, assuming that the electric field is known at a specific point, such as the conductor surface, and was then compared with 2D numerical simulations with in-plane currents. The results showed that the alternating current distribution in the coke bed is strongly influenced by the (parallel) currents in the metal. Hence, depending on the furnace size and the internal material distribution, there can be significant differences between the power distributions for 50 Hz AC compared to DC [16,17].

As with the furnace hearth, a simplified model can provide a practical and computationally efficient approach to understanding inductive effects in the layered materials that make up the furnace lining and steel casing. Accurate assessment of the electric field and power distribution is essential for designing these components to withstand harsh operating environments while maintaining efficiency. In this work, a general 1D model applicable to N material layers with varying electrical conductivity and magnetic permeability is described and solved. The model determines the distribution of the electric field across the layered media, either based on a known field value at a point, such as the conductor surface, or by specifying the total cross-sectional current per unit length. An approximate solution is derived for a specific two-layer scenario where an adjacent layer exhibits very good conductivity. The model is further applied to a layered system mimicking the casing and shell configuration of a submerged arc furnace (cf. Fig. 8) under the assumption that the current is vertical in that part. Thus, the 1D approach is exploited to study vertical currents in the lining and steel shell. The results are compared with 2D numerical simulations with out-of-plane currents to validate the effectiveness of the model. While the induction process is governed by the three electrode currents, the 1D model is designed to calculate induced currents in areas not directly connected to the current source, where a 1D approximation is appropriate. The boundary conditions for this low-dimensional model should somehow be obtained from 2D or 3D approximations.

The search for analytical formulas to solve electromagnetic problems is still an active area of research because of their much shorter computation time. For instance, in [18,19] different proposals are given to compute the induced losses in axially symmetric conductors consisting of several concentric layers due to harmonic external electromagnetic sources. Our 1D model is inspired by the analysis performed in [20] with the novelty of treating several types of boundary conditions and focusing on the low frequency case. Furthermore, to the best of the authors' knowledge, the application of such techniques to the analysis of the inductive effects in metallurgical applications has not been addressed before.

2. Mathematical model

The electromagnetic fields are governed by Maxwell's equations. In submerged arc furnaces, which operate with low-frequency alternating currents (typically around 50 - 60 Hz) without charge accumulation and assuming linear magnetic properties of the materials, the well-established time-harmonic eddy current approach can be used for the analysis (see, for example, [21]). This model reads:

$$i\omega\mathbf{B} + \mathbf{curl}\ \mathbf{E} = \mathbf{0}, \tag{2.1}$$

$$\mathbf{curl}\ \mathbf{H} = \mathbf{J}, \tag{2.2}$$

$$\mathrm{div}\ \mathbf{B} = 0, \tag{2.3}$$

$$\mathrm{div}\ (\varepsilon\mathbf{E}) = 0, \tag{2.4}$$

$$\mathbf{B} = \mu\mathbf{H}, \tag{2.5}$$

$$\mathbf{J} = \sigma\mathbf{E}, \tag{2.6}$$

where $\mathbf{E}$, $\mathbf{B}$, $\mathbf{H}$ and $\mathbf{J}$ are the complex amplitudes (or phasors) associated with the electric field, magnetic induction, magnetic field and electric current, respectively. That is, the fields of the full solutions can be written on the form $\mathcal{G}(\mathbf{x}, t) = \mathrm{Re}\left[\mathbf{G}(\mathbf{x})\exp(i\omega t)\right]$, where $\mathbf{x} \in \mathbb{R}^3$ is the spatial variable, $\omega = 2\pi f$ the angular frequency associated with the AC frequency f, and i is the imaginary unit. As usual, σ is the electrical conductivity of the material, ε the electrical permittivity and μ its magnetic permeability given by $\mu = \mu_0\mu_r$, with μ_r the relative magnetic permeability of the material and μ_0 the vacuum permeability.

Let us consider a 2D rectangular conductor with thickness T and width W with constant electromagnetic material properties defined by $(\sigma, \mu, \varepsilon)$. The conductor lies in the Cartesian yz-plane and it carries an alternating current with frequency f flowing in this plane.

From the time-harmonic Maxwell's equations presented above, one can derive a single equation governing the $\mathbf{E}$-field in the conductor in a similar way to the classical wave equations of electrodynamics [22]. By taking the **curl** operator of (2.1), inserting (2.2) and (2.5), the following equation is obtained

$$\mathbf{curl}(\mathbf{curl}\ \mathbf{E}) + i\omega\mu\sigma\mathbf{E} = \mathbf{0}. \tag{2.7}$$

Then, using the vector identity **curl** (**curl** $\mathbf{E}$) = **grad** (div $\mathbf{E}$) − div (**grad** $\mathbf{E}$) and that div $\mathbf{E} = 0$ for constant ε, the previous equation can be rewritten as

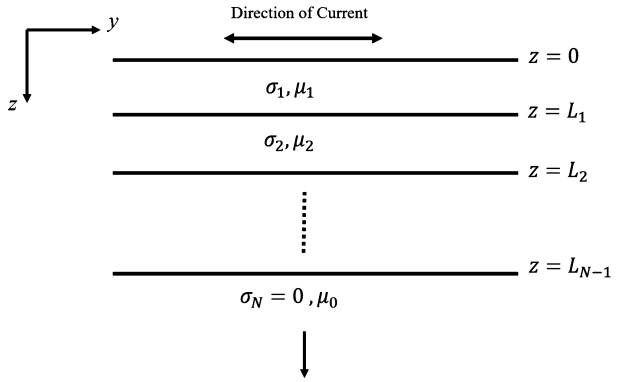

Fig. 2. Schematic representation of a 1D domain with N layers.

$$\text{div}\,(\mathbf{grad}\,\mathbf{E}) - \frac{2i}{\delta^2}\mathbf{E} = \mathbf{0}. \tag{2.8}$$

Here, δ denotes the skin depth defined as $\delta = 1/\sqrt{\pi f \sigma \mu}$.

By explicitly writing the 2D div-**grad** operator, (2.8) reads

$$\frac{\partial^2}{\partial y^2}\mathbf{E}(y,z) + \frac{\partial^2}{\partial z^2}\mathbf{E}(y,z) - \frac{2i}{\delta^2}\mathbf{E}(y,z) = \mathbf{0}. \tag{2.9}$$

Let us introduce the non-dimensional variables indicated by a tilde as:

$$y = W\tilde{y}, \quad z = T\tilde{z}, \quad \mathbf{E} = E_c\tilde{\mathbf{E}},$$

where E_c is a characteristic field value such as, for instance, the maximum field strength at the conductor surface. Thus, the wave equation (2.9) can be written in terms of non-dimensional variables as

$$\frac{1}{W^2}\frac{\partial^2}{\partial \tilde{y}^2}\tilde{\mathbf{E}}(\tilde{y},\tilde{z}) + \frac{1}{T^2}\frac{\partial^2}{\partial \tilde{z}^2}\tilde{\mathbf{E}}(\tilde{y},\tilde{z}) - \frac{2i}{\delta^2}\tilde{\mathbf{E}}(\tilde{y},\tilde{z}) = \mathbf{0}. \tag{2.10}$$

Note that, in (2.10), the function $\tilde{\mathbf{E}}(\tilde{y},\tilde{z})$ is non-dimensional, while the coefficient in each term has units of $1/\text{m}^2$. Furthermore, the intensity E_c has disappeared from the equation as it is a common factor in all terms. This shows that the intensity is a scaling factor, determining the absolute value of the solution, while the qualitative behaviour is given by the remaining parameters.

The equation is written in non-dimensional form by multiplying it by a quantity with the unit m^2. All four coefficients in (2.10) can be used for this purpose. Depending on the particular problem, it will be natural to consider multiplication by W^2 or T^2. Multiplying the equation (2.10) by T^2 gives

$$\left(\frac{T}{W}\right)^2\frac{\partial^2}{\partial \tilde{y}^2}\tilde{\mathbf{E}}(\tilde{y},\tilde{z}) + \frac{\partial^2}{\partial \tilde{z}^2}\tilde{\mathbf{E}}(\tilde{y},\tilde{z}) - 2i\left(\frac{T}{\delta}\right)^2\tilde{\mathbf{E}}(\tilde{y},\tilde{z}) = \mathbf{0}. \tag{2.11}$$

Now, consider a scenario where only the component $\tilde{E}_y$ is significant because the current is mainly in the y-direction; notice that the same analysis applies to $\tilde{E}_z$ in the opposite case where $\tilde{E}_y = 0$. Moreover, for "long and thin" conductors where the ratio of thickness to width satisfies $(T/W)^2 \ll 1$, the first term in (2.11) can be neglected. In this case, by reintroducing the dimensional variable $z = T\tilde{z}$, the governing equation for the electric field is reduced to an analytically solvable differential equation:

$$\frac{d^2}{dz^2}E_y(z) - \frac{2i}{\delta^2}E_y(z) = 0. \tag{2.12}$$

In the following section, we will present a solution to equation (2.12) for a generalized problem involving layers of adjacent conducting materials. This layout could represent the different layers of materials in a smelting furnace and be used to study the distribution of the electric field in conducting materials and how regions with different material properties affect each other. A similar setup was studied in [20], focusing on electromagnetic waves in the radio frequency domain and investigating the "effective skin depth" in coated conductors. The authors treated the inner layer as a base conductor with high conductivity that dampens the field to zero. The motivation and derivation for the model presented here are different. Given the focus on electrical furnaces operating at low-frequency AC, only the low-frequency solution is relevant here, thus simplifying the model and its corresponding solution.

2.1. General 1D model

Let us consider a medium with N layers, with $N \geq 3$, as depicted in Fig. 2. This could represent a cross section $z = z_0$ of the 3D model including the various lining layers and the steel shell as depicted in Fig. 8. The materials are located in the infinite half-plane $z \geq 0$ and an alternating current flows parallel to the layers in the y-direction. We assume that the first $N-1$ layers are conductors

defined by their electromagnetic properties $\sigma_j > 0$ and μ_j, while the N-th layer is a dielectric of infinite thickness with the properties $\sigma_N = 0$ and $\mu_N = \mu_0$. The interface between the j-th and $j+1$-th materials is denoted by L_j, so that the j-th material occupies the interval $L_{j-1} \leq z < L_j, j = 1 \ldots N-1$ (with $L_0 = 0$), while the N-th layer occupies the region $z \geq L_{N-1}$. As material properties are included in the equation, (2.12) must be solved for each layer individually. For $j = 1, \ldots, N-1$, the general solution is given by

$$E_j(z) = A_j e^{-\alpha z/\delta_j} + B_j e^{\alpha z/\delta_j}, \quad \text{for } L_{j-1} \leq z < L_j, \tag{2.13}$$

where $\alpha = 1 + i$ and δ_j is the skin depth associated with the j-th layer. For the dielectric layer ($j = N$), the governing equation reduces to

$$\frac{d^2}{dz^2} E_N(z) = 0, \tag{2.14}$$

which has the general solution

$$E_N(z) = A_N z + B_N, \quad \text{for } z \geq L_N. \tag{2.15}$$

This results in a set of N equations with $2N$ unknown coefficients (A_j, B_j). The interface conditions supplies $2(N-1)$ equations. One additional condition is then needed. Several options are possible. The obvious one is to specify E_0, the value of the parallel **E**-field at the surface. In addition, we will consider the case where the total (horizontal) current is given. We enforce the condition that the field remains bounded everywhere implying $A_N = 0$. Assuming no charge accumulation or surface currents, the tangential components of the electric field **E** and the magnetic field **H** are continuous at the interface between adjacent materials. By applying Ampere's law (2.2) the latter can be expressed in terms of the electric field as explained in the sequel.

2.1.1. Solution with known electric field at the surface

Let us first assume that the electric field at the surface, E_0, is known. In this case, the boundary and interface conditions can be summarized as follows

$$E(z) = E_0 \qquad \text{at } z = 0, \tag{2.16}$$

$$E_j(z) = E_{j+1}(z) \qquad \text{at } z = L_j, \tag{2.17}$$

$$\frac{1}{\mu_j}\frac{d}{dz} E_j(z) = \frac{1}{\mu_{j+1}}\frac{d}{dz} E_{j+1}(z) \qquad \text{at } z = L_j, \tag{2.18}$$

$$|E(z)| < C \qquad \forall z, \tag{2.19}$$

where C is a positive constant and $j = 1, \ldots, N-1$. By applying these conditions to the expressions (2.13) and (2.15), the coefficients $A_j, B_j, j = 1, \ldots, N$ can be determined, yielding

$$A_1 = \frac{E_0}{1 + \frac{\beta_1/\gamma_1 - 1}{\beta_1/\gamma_1 + 1} e^{-2\alpha L_1/\delta_1}}, \tag{2.20}$$

$$A_j = A_{j-1} \frac{2}{\gamma_{j-1} + \beta_{j-1}} e^{-\alpha L_{j-1}/\delta_{j-1}} \qquad j = 2, \ldots, N-1, \tag{2.21}$$

$$A_N = 0 \tag{2.22}$$

$$B_j = A_j \frac{\beta_j/\gamma_j - 1}{\beta_j/\gamma_j + 1} e^{-2\alpha L_j/\delta_j} \qquad j = 1, \ldots, N-2, \tag{2.23}$$

$$B_{N-1} = A_{N-1} e^{-2\alpha L_{N-1}/\delta_{N-1}}, \tag{2.24}$$

$$B_N = 2A_{N-1} e^{-\alpha L_{N-1}/\delta_{N-1}}, \tag{2.25}$$

where, for $N > 3$, the constants β_j and γ_j $(j = 1, \ldots, N-2)$ have been introduced. These constants are, in turn, determined recursively by

$$\beta_j = e^{-\alpha L_j/\delta_{j+1}} + \frac{\beta_{j+1}/\gamma_{j+1} - 1}{\beta_{j+1}/\gamma_{j+1} + 1} e^{\alpha(L_j - 2L_{j+1})/\delta_{j+1}}, \tag{2.26}$$

$$\gamma_j = \frac{\delta_j}{\delta_{j+1}} \frac{\mu_j}{\mu_{j+1}} \left(e^{-\alpha L_j/\delta_{j+1}} - \frac{\beta_{j+1}/\gamma_{j+1} - 1}{\beta_{j+1}/\gamma_{j+1} + 1} e^{\alpha(L_j - 2L_{j+1})/\delta_{j+1}} \right), \tag{2.27}$$

for $j = N-3, \ldots, 1$, given that β_{N-2} and γ_{N-2} can be computed beforehand as

$$\beta_{N-2} = e^{-\alpha L_{N-2}/\delta_{N-1}} + e^{\alpha(L_{N-2} - 2L_{N-1})/\delta_{N-1}}, \tag{2.28}$$

$$\gamma_{N-2} = \frac{\delta_{N-2}}{\delta_{N-1}} \frac{\mu_{N-2}}{\mu_{N-1}} \left(e^{-\alpha L_{N-2}/\delta_{N-1}} - e^{\alpha(L_{N-2} - 2L_{N-1})/\delta_{N-1}} \right). \tag{2.29}$$

Since the electric field is bounded, then $A_N = 0$ (2.22), which implies that the electric field within the dielectric layer is constant. The above expressions show that A_1 is determined from E_0 and the material properties. For $j = 1, \dots, N-1$, the remaining values are then obtained from A_1. This recursive procedure for computing the solution is easily implemented for a general number of layers by simply knowing the positions of the interfaces and the conductivities and permeabilities of the different materials.

Once the electric field distribution has been determined, the current $J_j(z)$ and the power density $p_j(z)$ can be calculated for each layer. The current density is computed using Ohm's law (2.6); the power density is calculated by taking the time average of the scalar product of the current density and electric field over one cycle of the AC current. In the harmonic regime, this integral yields $|\mathbf{J}|^2/(2\sigma)$ (see, for instance, [21]). Then, for $j = 1, \dots, N-1$, straightforward calculations provide

$$J_j(z) = \sigma_j \left(A_j e^{-\alpha z/\delta_j} + B_j e^{\alpha z/\delta_j} \right), \tag{2.30}$$

$$p_j(z) = \frac{\sigma_j}{2} \left[|A_j|^2 e^{-2z/\delta_j} + |B_j|^2 e^{2z/\delta_j} + 2\,\mathrm{Re}\left(A_j \bar{B}_j e^{-2iz/\delta_j} \right) \right], \tag{2.31}$$

with $\bar{B}_j$ the complex conjugate of B_j. The total dissipated power, P_j, in the j-th layer is found by evaluating the integral of $p_j(z)$ from L_{j-1} to L_j, which gives

$$P_j = \frac{\sigma_j \delta_j}{4} \left[-|A_j|^2 \left(e^{-2L_j/\delta_j} - e^{-2L_{j-1}/\delta_j} \right) + |B_j|^2 \left(e^{2L_j/\delta_j} - e^{2L_{j-1}/\delta_j} \right) + 2\,\mathrm{Re}\left(iA_j \bar{B}_j \left(e^{-2iL_j/\delta_j} - e^{-2iL_{j-1}/\delta_j} \right) \right) \right]. \tag{2.32}$$

2.1.2. Alternative formulation with known total current

A similar general solution can be obtained for the alternative case where the total electric current per unit length, I_{tot}, through the conductor is known. This approach requires the expression (2.20) for A_1 to be rewritten as a function of I_{tot}. After this step, the same recursive expressions as those obtained above can be utilized to determine the remaining parameters.

The total current per unit length, I_{tot}, is related to the electric field distribution by an integral over the current density in the conducting domain. This integral can be expressed as the sum of the integrals for each layer, which, considering Ohm's law, gives

$$I_{tot} = \sum_{j=1}^{N-1} \int_{L_{j-1}}^{L_j} \sigma_j E_j(z)\, dz. \tag{2.33}$$

This expression replaces the boundary condition (2.16) used in the previous case, while conditions (2.17)-(2.19) remain unchanged. Taking into account the general solution for the electric field in each layer we can write

$$I_{tot} = \sum_{j=1}^{N-1} \frac{\sigma_j \delta_j}{\alpha} \Big(-A_j \left[e^{-\alpha L_j/\delta_j} - e^{-\alpha L_{j-1}/\delta_j} \right] + B_j \left[e^{\alpha L_j/\delta_j} - e^{\alpha L_{j-1}/\delta_j} \right] \Big). \tag{2.34}$$

The recursive relations (2.20)-(2.25) for finding the coefficients A_j and B_j, as given in previous section, are still valid. Moreover, for all j, equations (2.20)-(2.29) can be employed to write $A_j = A_1 \widehat{A}_j$ and $B_j = A_1 \widehat{B}_j$, with $\widehat{A}_1 = 1$. Thus, (2.34) yields

$$I_{tot} = A_1 \sum_{j=1}^{N-1} \frac{\sigma_j \delta_j}{\alpha} \Big(-\widehat{A}_j \left[e^{-\alpha L_j/\delta_j} - e^{-\alpha L_{j-1}/\delta_j} \right] + \widehat{B}_j \left[e^{\alpha L_j/\delta_j} - e^{\alpha L_{j-1}/\delta_j} \right] \Big)$$

and solving for A_1 gives

$$A_1 = I_{tot} \Big[\sum_{j=1}^{N-1} \frac{\sigma_j \delta_j}{\alpha} \Big(-\widehat{A}_j \left[e^{-\alpha L_j/\delta_j} - e^{-\alpha L_{j-1}/\delta_j} \right] + \widehat{B}_j \left[e^{\alpha L_j/\delta_j} - e^{\alpha L_{j-1}/\delta_j} \right] \Big) \Big]^{-1}.$$

The expressions for $\widehat{A}_j$ and $\widehat{B}_j$ can be obtained using equations (2.21), (2.23), and (2.24). Specifically,

$$\widehat{A}_j = \prod_{k=1}^{j-1} \frac{2}{\gamma_k + \beta_k} e^{-\alpha L_k/\delta_k}, \quad \text{for } j = 2, \dots, N-1, \tag{2.35}$$

$$\widehat{B}_j = \widehat{A}_j \frac{\beta_j/\gamma_j - 1}{\beta_j/\gamma_j + 1} e^{-2\alpha L_j/\delta_j}, \quad \text{for } j = 1, \dots, N-2, \tag{2.36}$$

$$\widehat{B}_{N-1} = \widehat{A}_{N-1} e^{-2\alpha L_{N-1}/\delta_{N-1}}, \tag{2.37}$$

where β_j and γ_j are defined in (2.26)-(2.29) depending on the value of j. Finally, the coefficients A_N and B_N are also the same as in the case where E_0 is known (see (2.22) and (2.25)).

Remark. The model can easily be extended to include dielectric layers or conductive layer at the bottom. For dielectric layers, (2.12) will be replaced by

$$\frac{d^2}{dz^2} E_j(z) = 0$$

Table 1
Parameters of 1D model example with $N = 5$ and $f = 50$ Hz.

Layer	T[m]	σ[S/m]	μ_r[−]	δ[m]
1	0.5	$5 \cdot 10^2$	1	3.18
2	0.5	$1.4 \cdot 10^4$	1	0.60
3	0.2	$1 \cdot 10^{-6}$	1	$7.1 \cdot 10^4$
4	0.2	$1 \cdot 10^6$	100	$7.1 \cdot 10^{-3}$
5	'∞'	0	1	–

Table 2
1D model example with $N = 5$. Dissipated power.

	$\mu_4 = \mu_0$		$\mu_4 = 100\mu_0$	
Layer	P_j [W]	P_j/P_{tot} [%]	P_j [W]	P_j/P_{tot} [%]
1	73.09	14	71.61	11
2	424.01	82	507.30	78
3	0	0	0	0
4	20.30	4	74.87	11
Total	517.40	100	653.78	100

with the solution

$$E_j(z) = \bar{A}_j z + \bar{B}_j, \quad \text{for } L_{j-1} < z < L_j$$

i.e., linear variation within the layer.

For a conductive layer at the bottom, (2.12) will be valid, with solution

$$E_N(z) = \bar{A}_N e^{-\alpha z/\delta_N} + \bar{B}_N e^{\alpha z/\delta_N}.$$

Here, $\bar{B}_N = 0$ since the field remains bounded everywhere.

In practical applications of the model, these two extensions do not need separate treatment. For dielectric layers, one can assume a very low conductivity. The solution given by (2.13) will approach linear variation as $\sigma_j \to 0$ ($\delta_j \to \infty$). For a bottom conductive layer, one can let the layer be finite, but very thick, $\delta \ll L$. Then, an extra dielectric layer can be added at the bottom. The E-field will now vanish within the thick conductive layer, and the formulas in sections 2.1.1 and 2.1.2 can be applied.

2.1.3. Example case with $N = 5$ layers; influence of magnetic permeability

In this example, we analyze a 1D model consisting of five layers with different properties, including insulators, moderate and very good conductors. The properties and thicknesses of each layer are detailed in Table 1, with values typical of those found in a submerged arc furnace, such as the coke bed, carbon lining, oxide lining, and steel shell. For illustrating purposes, the steel shell is unrealistic thick. The example considers magnetic and non-magnetic casing. The former is modelled as a linear material with permeability $\mu_4 = 100$, while $\mu_4 = 1$ for the latter. For both cases the computations have been normalized by letting $E(0) = 1$ V/m at a frequency of $f = 50$ Hz.

Fig. 3 shows the distributions of the electric field, current density and power density. In particular, the electric field transition at the surface of the magnetic material is not smooth, while both the current and power densities show discontinuities at the material boundaries due to conductivity jumps.

Table 2 shows the total power dissipated in each layer. In this example, the conductive layers generate a total power dissipation of approximately 654 W, with the second layer being the largest contributor, accounting for 78% of the total power. To explore the effect of magnetic permeability, the test was repeated by changing the relative magnetic permeability (μ_4) of the fourth layer from 1 to 100. As a result, the power dissipated in this layer and the total dissipated power increased significantly. The resulting distributions of electric field, current density and power density are also shown in Fig. 3.

2.2. An approximate solution for a conductor adjacent to a highly conductive material

In many applications there are scenarios where a moderately or poorly conducting material is adjacent to a highly conducting one. In submerged arc furnaces, examples include materials adjacent to electrodes, the coke bed above the alloy, or the furnace lining within the steel shell [16]. This section aims to provide an approximate solution to the general 1D model for a two-layer problem where the inner layer is highly conductive. In such cases, the electric field quickly decays to zero, so the treatment can be simplified by treating the layer as infinitely thick. The first layer is assumed to have thickness T and conductivity σ_1, while the second layer has conductivity σ_2. The analysis assumes a known total current per unit length, I_{tot}, and examines the behaviour of the two-layer system as the conductivity of the inner layer approaches infinity.

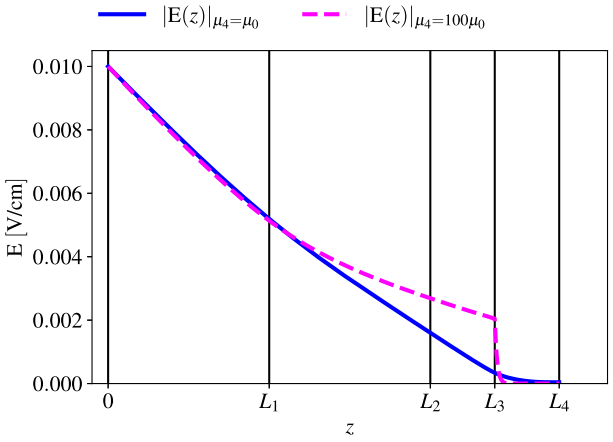

(a) Modulus of the electric field.

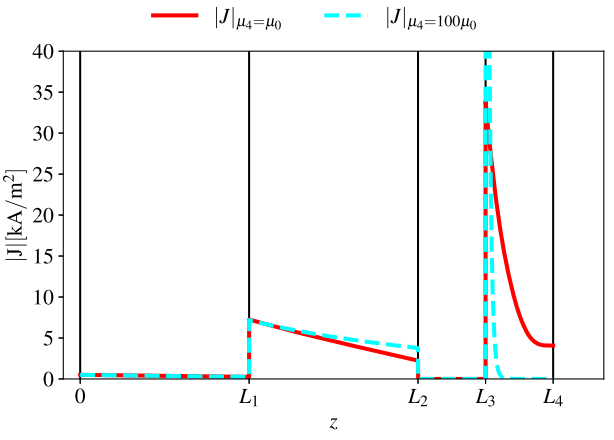

(b) Modulus of the current density.

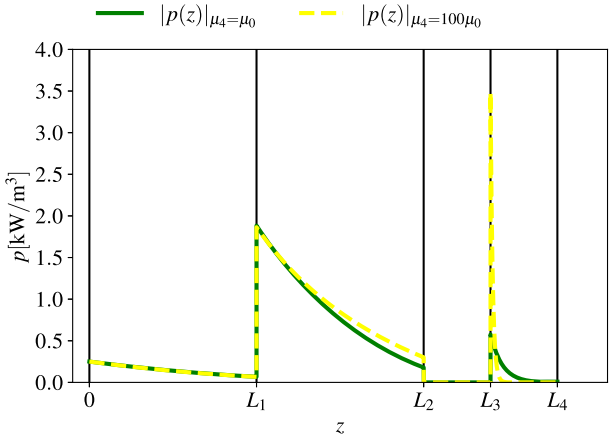

(c) Power density.

Fig. 3. Five-layered material example. The cases $\mu_4 = 100\mu_0$ and $\mu_4 = \mu_0$ are compared.

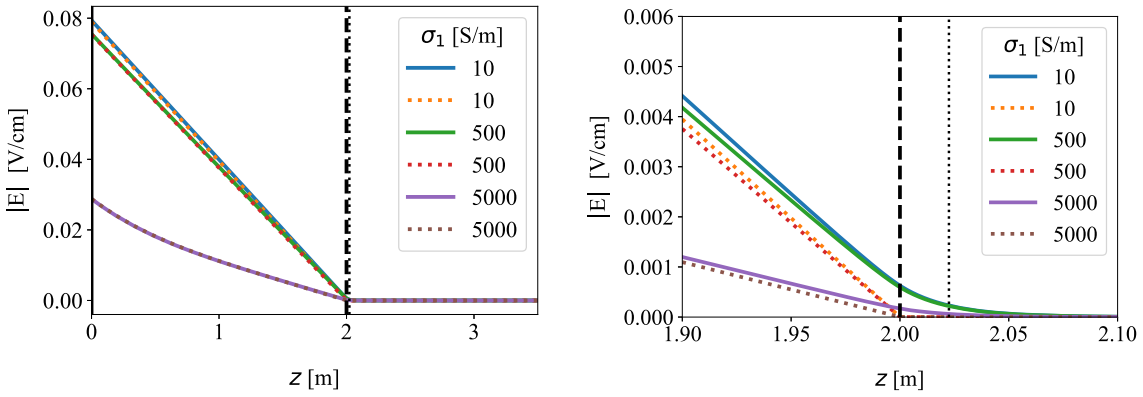

(a) $|E(z)|$ in two layers. (b) Zoom at the material interface.

Fig. 4. Electric field distribution in two layers as calculated by the full analytical (solid lines) and approximate (dashed) solutions. σ_1 takes three different values, while σ_2 is fixed. The total applied current is 50 Hz AC with an amplitude of 1 A. The vertical dotted line at $z = 2.0225$ m represents the skin depth of the second material.

2.2.1. *Derivation of the model and validation*

The general solution for the electric field distribution for this two-layer problem is given by

$$E_1(z) = A_1 e^{-\alpha z/\delta_1} + B_1 e^{\alpha z/\delta_1} \qquad \text{for } 0 \le z \le T, \tag{2.38}$$

$$E_2(z) = A_2 e^{-\alpha z/\delta_2} + B_2 e^{\alpha z/\delta_2} \qquad \text{for } z \ge T. \tag{2.39}$$

Since the electric field is bounded, it follows that $B_2 = 0$. The remaining unknown coefficients can be obtained in the same way as the general recursive set up for N layers. Furthermore, by applying the interface conditions, both B_1 and A_2 can be written in terms of A_1 as $B_1 = \breve{B}_1 A_1$ and $A_2 = \breve{A}_2 A_1$ where:

$$\breve{B}_1 = \frac{\mu_2\delta_2 - \mu_1\delta_1}{\mu_2\delta_2 + \mu_1\delta_1} e^{-2\alpha T/\delta_1}, \tag{2.40}$$

$$\breve{A}_2 = 2\frac{\mu_2\delta_2}{\mu_2\delta_2 + \mu_1\delta_1} e^{-\alpha T(1/\delta_1 - 1/\delta_2)}. \tag{2.41}$$

Finally, given the total current, A_1 is computed as

$$A_1 = \frac{\alpha I_{tot}}{\sigma_1\delta_1\left(\breve{B}_1(e^{\alpha T/\delta_1} - 1) - e^{-\alpha T/\delta_1} + 1\right) + \sigma_2\delta_2\breve{A}_2 e^{-\alpha T/\delta_2}}. \tag{2.42}$$

The solution to the two-layer problem is obtained by substituting the expression for A_1 as well as those of B_1 and A_2 as a functions of A_1 in (2.38) and (2.39).

Let us now explore the scenario where the second layer is highly conductive, i.e. when δ_2 approaches zero. Assuming for simplicity that both materials have equal permeabilities ($\mu_1 = \mu_2$), evaluating the limits for $\breve{B}_1$ and $\breve{A}_2$ yields

$$\lim_{\delta_2 \to 0} \breve{B}_1 = -e^{-2\alpha T/\delta_1}, \tag{2.43}$$

$$\lim_{\delta_2 \to 0} \breve{A}_2 = 0, \tag{2.44}$$

which gives the limit for A_1 as

$$\lim_{\delta_2 \to 0} A_1 = \pi f \mu_0 \alpha I_{tot} \frac{\delta_1}{e^{-2\alpha T/\delta_1} + 1}. \tag{2.45}$$

This approximate solution considers $E_2(z)$ to be zero and $E_1(z)$ to depend only on the material properties of the first layer. Fig. 4 shows three example cases solved using both the full analytical solution and the approximate solution. Each case varies σ_1 while keeping other parameters constant: $\sigma_2 = 10^7$ S m^{-1}, $T = 2$ m, $\mu_1 = \mu_2 = \mu_0$, total cross section current of 1 A, and frequency $f = 50$ Hz. For σ_1 values of 50, 500 and 5000 S m^{-1} are considered, corresponding to skin depths δ_1 of 10.1, 3.18 and 1.01 m respectively. These values are representative of materials typically found in metallurgical furnaces. The approximate solution forces the electric field in the second region to be zero ($\breve{A}_2 = 0$), leading to a systematic error in the solution. This error decreases with increasing conductivity (σ_1) as the field tends to zero in layer 1. This phenomenon is illustrated in Fig. 4b, which shows the same curves as Fig. 4a, but focuses on a small region around the material interface.

The approximate solution is compared numerically with the analytical solution by evaluating the relative difference between the two solutions in the first layer, defined as

Table 3
Difference between approximate and full solution: Relative error Δ_1 for some values of σ_1 and σ_2.

σ_1 [S/m]	σ_2 [S/m]	Δ_1
50	10^7	0.0157
500	10^7	0.0151
5000	10^7	0.0064
50	10^8	0.0050
500	10^8	0.0048
5000	10^8	0.0021

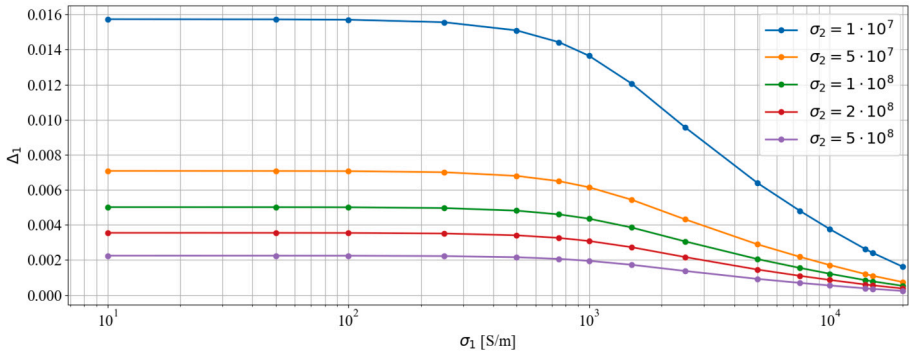

Fig. 5. Difference between approximate and full solutions: values of the relative error Δ_1 vs. σ_1 for different values of σ_2.

$$\Delta_1 = \frac{\int_0^T |E_{full}(x) - E_{app}(x)|dx}{\int_0^T |E_{full}(x)|dx}, \tag{2.46}$$

where E_{full} is the full solution (in material 1) as given by the coefficients in equations (2.40), (2.41) and (2.42), while E_{app} is the approximate solution given by the coefficients in (2.43), (2.44) and (2.45). Table 3 shows the values of Δ_1 for each of the three cases presented in Fig. 4, as well as for the same three values of σ_1 but with σ_2 increased by a factor of 10. The values show that for the given setup the errors tend to decrease as σ_1 increases. This is due to the fact that the skin depth of the first layer is reduced so that the field is more attenuated before the interface where it is forced to zero by the approximate solution. We also see that the overall error is smaller as σ_2 increases, as one would expect. The decaying error with increasing σ_1 is also shown in Fig. 5, which plots the error integral as a function of σ_1 for five different cases of σ_2.

2.2.2. *Distribution of current and power*

In this section, we will further explore the approximate solution and investigate the distribution of current between the two layers, as well as the resulting total power generated. Since the approximate solution yields a zero electric field in the highly conductive layer, the power generated in this layer will consequently be zero as well. But we cannot preclude a current in this layer.

We will now focus on analyzing the behaviour of the total power P_1 generated in the outer layer (σ_1) with respect to changes in material properties and thickness. Using the approximate expressions for $\hat{B}_1$ and A_1 derived in (2.40) and (2.42), respectively, the total current through the cross section in material 1 is given by

$$I_1 = I_{tot} \frac{\left(e^{-\alpha T/\delta_1} - 1\right)^2}{e^{-2\alpha T/\delta_1} + 1}, \tag{2.47}$$

showing that I_1 generally differs from I_{tot}. As $E_2 = 0$, it does not make sense to define a distributed current I_2. Instead, we define a surface current I_T flowing in the infinitesimal skin layer of material 2:

$$I_T = I_{tot} - I_1 = I_{tot}\left(1 - \frac{\left(e^{-\alpha T/\delta_1} - 1\right)^2}{e^{-2\alpha T/\delta_1} + 1}\right). \tag{2.48}$$

The real parts of these expressions are plotted in Fig. 6 for different values of δ_1/T. As expected, for small values of δ_1/T, layer 1 is a very good conductor and all current flows in this layer. Conversely, for large values of δ_1/T, the layer is a very poor conductor and all current flows at the surface of the very good conductor (material 2). Between these two extremes, an interesting behaviour occurs: for a range of values of $\delta_1/T \sim 1$, the total current in material 1, I_1, exceeds the applied total current I_{tot}, while simultaneously a reverse current appears in material 2. This is interpreted as a consequence of normal induction: when there is AC in layer 1, layer 2 responds

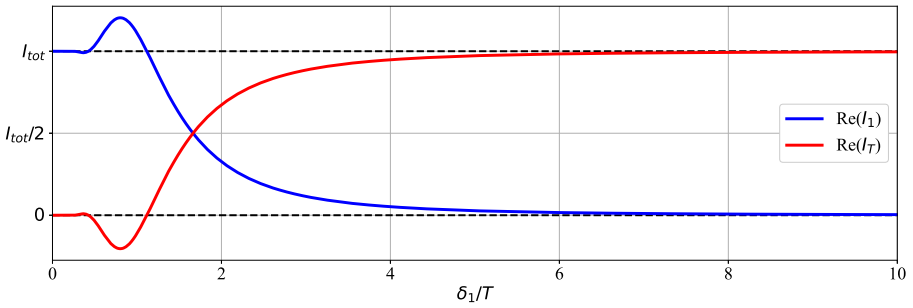

Fig. 6. Approximate solution depending on the skin depth in layer 1. Blue: real part of the total current in layer 1. Red: real part of the total line current at the interface $z = T$.

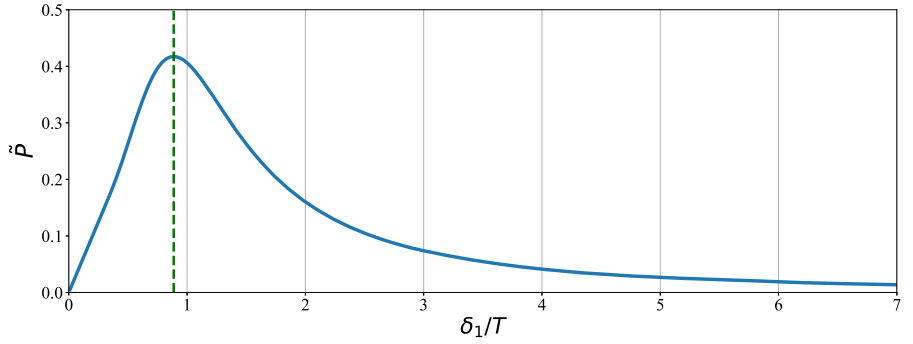

Fig. 7. Non-dimensional power in material layer 1 as a function of δ_1/T. The vertical line indicates the maximum of the function.

with an induced current in the opposite direction. For increasing values of δ_1/T, the current prefers to flow without resistance at the boundary, until all current is found here.

In regard to the power, since E_2 is zero, there is no power associated with material 2. To analyze the total power in material 1, we introduce non-dimensional variables as follows:

$$z = T\tilde{z}, \qquad \sigma(z) = \sigma_1\tilde{\sigma}(\tilde{z}), \qquad E(z) = \frac{I_{tot}}{\sigma_1 T}\tilde{E}(\tilde{z}). \tag{2.49}$$

Here z is scaled by the thickness T of the first layer and σ by σ_1, while the electric field is scaled by the total current I_{tot}, the conductivity σ_1 and T. This choice for the electric field is natural when the total current is given, or can be properly estimated, for instance due to induction.

Using the non-dimensional variables and considering the definition of $\breve{B}_1$ in (2.40), the non-dimensional power density in material 1 can be expressed as

$$\tilde{p}_1(\tilde{z}) = \frac{1}{2}\left(\frac{T\sigma_1}{I_0}\right)^2 |A_1|^2 \left[e^{-(2T/\delta_1)\tilde{z}} + |\breve{B}_1|^2 e^{(2T/\delta_1)\tilde{z}} + 2\,\mathrm{Re}\left(\bar{\breve{B}}_1 e^{-(2iT/\delta_1)\tilde{z}}\right)\right]. \tag{2.50}$$

The total non-dimensional power $\tilde{P}_1$ in the first material is then obtained by evaluating the integral of $\tilde{p_1}(\tilde{z})$ from 0 to 1. In the approximation where δ_2 tends to 0, this gives

$$\lim_{\delta_2 \to 0} \tilde{P}_1 = \frac{1}{4}\frac{\delta_1}{T}\left|\frac{\alpha}{e^{-2\alpha T/\delta_1} + 1}\right|^2 \left(-e^{-2T/\delta_1} + e^{-4T/\delta_1} + 2\,\mathrm{Re}\left[ie^{2\bar{\alpha}T/\delta_1}\right]\right). \tag{2.51}$$

Note that this expression is a function of the ratio between δ_1 and T, which are the only physical quantities in the expression. It is plotted as a function of the ratio δ_1/T in Fig. 7. The curve has a distinct maximum and decays rapidly on both sides near the maximum. For small values of δ_1/T, the expression reduces to $\delta_1/2T$, consistent with the almost linear slope below the maximum. The maximum point has been numerically determined to be $\delta_1/T = 0.88724$. In cases where our model is a reasonable approximation, Fig. 7 shows that the total generated electric power depends strongly on the value δ_1/T, with a maximum to be expected around $\delta_1/T = 0.9$.

3. Numerical simulations/ 1D model applied to the linings and casing of SAFs

In this section, we use the general analytical 1D model to analyze the electromagnetic field distribution within the linings and steel shell of a SAF. We compare these results with numerical simulations performed using a 2D out-of-plane model in COMSOL Multiphysics® finite element software, and in particular, with the AC/DC module [23]. The geometry of the 2D model, shown in

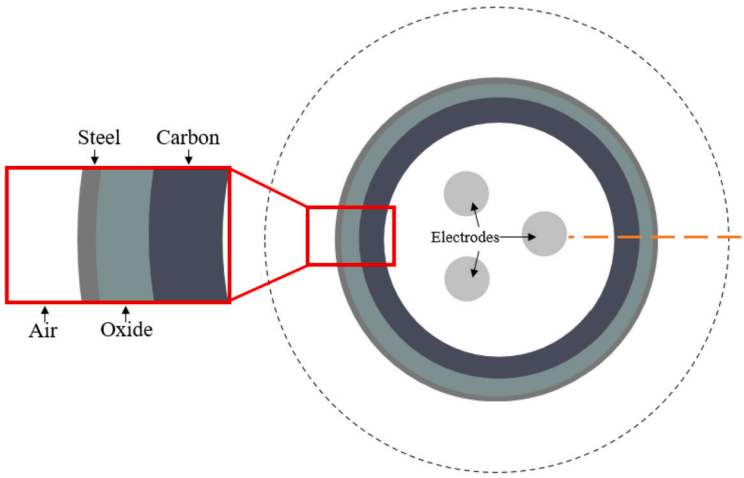

Fig. 8. 2D geometry including an enlarged detail of the linings and steel shell.

Table 4
Material properties [12] and layer thickness for the furnace casing model; the skin depth is given for $f = 50$ Hz.

Material	T [m]	σ [S/m]	μ_r [-]	δ [m]
Carbon	0.5	$1.4 \cdot 10^4$	1	0.60
Oxide	0.2	$1 \cdot 10^{-6}$	1	$7.1 \cdot 10^4$
Magnetic Steel	0.025	$3 \cdot 10^6$	100	0.0041
Non-Magnetic Steel	0.025	$1 \cdot 10^6$	1	0.71

Fig. 8, represents a horizontal section of the full 3D model (cf. Fig. 1) including all three electrodes, an inner charge material, various lining layers, and the steel shell. The dashed circle outlines the air included in the numerical computations. The main assumption of the 2D model is that the domains are infinite in the z-direction and the current density only has non-null component in such direction, that is, $\mathbf{J} = J_z(x, y)\mathbf{e}_z$. Hence, the model is applied in the upper part of the furnace, above the coke beds, where most of the current flows vertically. For a detailed description of the 2D model setup, we refer the reader to [10], where two and three-dimensional simulations are conducted to analyze induced currents in the lining and steel shell of three-phase SAFs. Note that the assumption of vertical current is also appropriate in the lining and steel shell if we neglect the current loops that flow horizontally in the upper part, as can be observed in 3D simulations. Similar models have also been used to study the proximity effect between the electrodes, and also the proximity effect between the electrodes and the steel shell [12,13,15].

In this study, we use the 1D model to analyze the area highlighted in Fig. 8, which includes a conductive carbon lining, an insulating oxide lining, the steel shell, and the surrounding air, forming a four-layer system. Since the 1D model presented above includes conducting materials except in the last layer, the oxide lining will be modelled as a very poor conducting material with extremely low electrical conductivity. To apply the 1D model we assume that the conductors are very long in the z-direction and the only non-null component of the electric field is the vertical one; moreover, we assume that the electric field only depends on the radial component r through the conducting layers.

Before comparing the 1D and 2D models, we verified that the results of the 2D FEM model were independent of mesh resolution by running simulations with different mesh sizes. Specifically, we used a reference mesh with a scale factor of 1, along with finer and coarser meshes corresponding to lower and higher scale factors, respectively. Table 5 shows the power dissipated in both the entire furnace and the carbon lining for each scale factor. As can be seen, the results converge to a consistent value as the mesh size decreases. In particular, a scale factor of 1 generates a mesh with 475 893 elements, while a scale factor of 0.55 results in 1 127 229 elements. Since using a finer mesh (scale factor < 1) does not significantly affect the results, we have selected the mesh with a scale factor of 1 for all subsequent analyses in this paper.

To compare the 1D and 2D models, we examine the radial distribution of the (vertical) electric field along the red dashed line in the figure. Two simulation cases were analyzed, differing in the magnetic properties of the steel shell: one with magnetic steel ($\mu_r = 100$) and the other with non-magnetic steel ($\mu_r = 1$). The electrical conductivity of the steel shell also varies, with $\sigma_s = 3 \cdot 10^6$ S/m for the magnetic case and $\sigma_s = 1 \cdot 10^6$ S/m for the non-magnetic one, reflecting different types of steel casings found in practical applications (see [12]). All materials are assumed to be magnetically linear. Table 4 summarizes the material properties and thickness of each layer used in the calculations, with the skin depth calculated at an AC frequency of 50 Hz.

Fig. 9 shows the radial electric field distribution (with $r = 0$ defined at the inner boundary of carbon lining) obtained from both the numerical 2D model and the analytical 1D model. The field value at the surface (E_0) is extracted from the numerical solution, sampled at the inner edge of the conductive carbon lining, and used as input for the 1D model. The sampling is performed behind

Table 5
Power in the furnace and in the carbon lining vs. the mesh size.

Scale factor	Furnace power [kW]	Carbon lining power [kW]
0.55	300.131	43.859
0.6	300.131	43.858
0.75	300.133	43.854
0.9	300.127	43.828
1	300.130	43.834
1.1	300.131	43.839
1.5	300.104	43.760
2	299.899	43.374
4	298.826	41.903

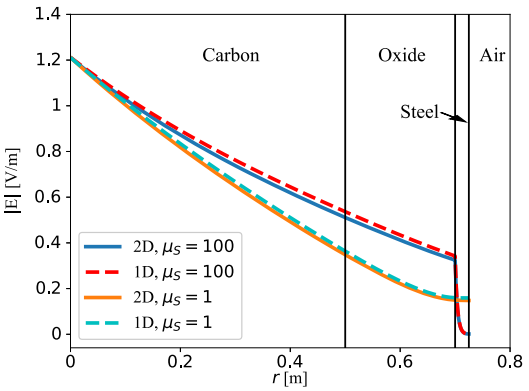

Fig. 9. Radial electric field distribution as calculated by the numerical 2D simulation (solid) and the analytical 1D model (dashed) for two cases with magnetic and non-magnetic steel.

Table 6
Deviation (Δ_1) of the radial electric field calculated by the analytical 1D model compared with 2D simulations for varying furnace diameters (D_F).

D_F [m]	7	8	9	10	11	12	13	14	15	16	18	20
Δ_1	0.058	0.047	0.039	0.034	0.030	0.026	0.024	0.022	0.020	0.018	0.016	0.014

one of the three electrodes, as indicated in the figure. The results demonstrate that the 1D model effectively captures the behaviour of the electric field for both simulation scenarios.

Note that due to the conservation of current, the total current in the three electrodes is zero at any given time ($I_{el_1} + I_{el_2} + I_{el_3} = 0$, I_{el_i} being the current at i-th electrode). According to Ampere's law, there will then be a net zero current induced in the surrounding conducting parts.

However, at any given radial transverse sector, vertical currents will be induced due to the high electrode currents and different distances to each electrode. Herland et al. [13] present an analytical solution for the case with infinitely thin electrodes and steel shell, with no other conducting materials present. This current in the steel shell can be applied as an approximation for the total current within any radial sector. In real life, the total current will deviate due to finite thickness of electrodes, lining and steel shell as well as the curvature of the furnace lining, but we expect that the basic properties will be captured by the simple model. To analyze the influence of curvature, we repeated the simulation shown in Fig. 9 for different furnace diameters, ranging from 7 to 20 meters. At the same time, we adjusted the distance between the electrodes to maintain a constant ratio between the "pitch circle diameter" (the circle passing through the centers of the three electrodes) and the furnace diameter. For each configuration, the thicknesses of the lining and shell were kept constant. We calculated the radial electric field distribution using both the 2D numerical simulation and the 1D analytical model, considering a non-magnetic steel shell case. By evaluating the relative error as defined in (2.46), we obtained the results summarized in Table 6. The results indicate that the fit to the 1D model improves with increasing furnace radius, as expected. In particular, for a furnace diameter of 13 meters (a typical size for industrial furnaces and used in our previous cases), the deviation between the models is minimal.

As mentioned above, the 1D model in the provided example relies on input data derived from the 2D simulations, which may introduce some uncertainty in the numerical results. However, as the example shows, the value E_0 is almost identical for the two cases. The main advantage of the 1D model is that it quickly provides a proper qualitative understanding. As shown in this example, it can be effectively used, for instance, to investigate the effect of modifying specific layer properties, as the ratio of the two distributions remains (approximately) independent of E_0. This is reasonable in situations like this where the value of E_0 is primarily determined by the applied electrode current and the distance to the conducting outer layers (carbon lining and steel shell) [13]. Therefore, this

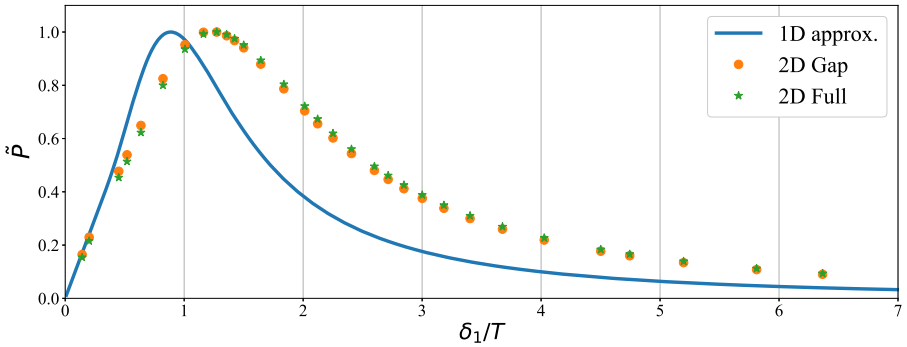

Fig. 10. Normalized total power dissipated in the carbon lining as a function of δ_1/T calculated with varying conductivity by the analytical 1D model (2.51) and by numerical 2D integrals over the full domain and a small section of the carbon lining.

shows that the change in electric field density and consequently the current and power distributions could have been estimated by the 1D model.

If the steel is considered a "very good" conductor, and the combined carbon and oxide linings are considered a moderately conductive layer, this model can also exemplify the approximate model outlined in Section 2.2.

It is of interest to investigate whether the qualitative behaviour described by (2.51) and illustrated in Fig. 7 can replicate the behaviour of the 2D model. To examine this, the 2D model was simulated with varied carbon lining conductivity, while keeping the remaining parameters constant according to Table 4, with non-magnetic steel in the shell. For each simulation, the total power generated in the carbon lining was computed by numerical integration in COMSOL. The integration was performed for the entire annulus representing the carbon lining and for a small section with an angular width of 0.1° placed centered behind an electrode, as shown in Fig. 8. The integration within a small section is adequate to compare the 1D model with the 2D simulations, as similar qualitative results are expected for each section. The integration of the entire annulus provides an average of all sections and is performed to verify that it behaves similarly to a single section. The results are shown in Fig. 10 as a function of δ_1/T along with the 1D approximated solution. Each of the curves has been normalized by dividing by its maximum value. The thickness of the carbon lining was kept constant at $T = 0.5$ m in each of the simulations. The values obtained from the numerical 2D integration show the same qualitative behaviour as the analytical 1D approximation, with a slight shift in the peak position. Some deviation from the analytical 1D model is expected due to the cylindrical geometry, the distributed electrodes and the design of the lining. One would expect the results from the small section closest to the electrode to be more similar to the analytical result, and they are. However, the discrepancy in peak position between the small section integral (orange) and the full integral (green) is insignificant. This example shows that the induced power in the lining will peak around $\delta_1/T = 1$, providing valuable information for the design of future furnace linings. It provides a semi-quantitative insight into how the amount of induced power will change due to changes in material data or thickness of the lining layers. Additional modelling, including a heat balance for the lining, is required to determine the optimum design.

4. Conclusions

A low-frequency 1D analytical model has been developed to characterize the electric field within layered conductors, with particular focus on metallurgical smelting furnaces. This model can determine the electric field distribution across a layered material by knowing either a single field value or the total cross-sectional current per unit length. It provides valuable insight into the mechanism of inductive effects between adjacent conductors and how the material properties of one material affect other materials in its vicinity. The distribution within a single layer of material is determined by the ratio of the skin depth of the material to the thickness of the layer.

By comparing the electric field distribution predicted by the 1D model with a numerically solved 2D model, we have shown that the 1D model gives a good estimate of the 2D solution. Thus, the physical mechanisms involved are adequately described by the 1D model.

In addition, a special case where a moderately conductive layer is adjacent to a very good conductor has been analyzed, an arrangement that can be related to several regions in a SAF, such as the steel shell surrounding the furnace lining. In this case, an approximate solution was derived that considers only the moderately conductive layer itself to determine the solution. This solution showed a distinct behaviour in the total power generated by the conductors, described by a simple expression in terms of the ratio δ/T, which has a clear maximum. Thus, for any thickness T, there is a given conductivity σ that gives the maximum amount of power dissipated. This behaviour has been further validated by numerical 2D calculations of the power dissipated in the carbon lining of submerged arc furnaces, confirming the effectiveness of the analytical model.

The 1D model can be used as a tool to better understand inductive effects for distributions through multiple material layers. It is easy to implement and analyze for any number of material layers, and can serve as an aid in the design of furnace linings or other applications where the current can be considered one-dimensional. Overall, the 1D model remains a valuable tool for qualitative

analysis and insight into the mechanisms at work in metallurgical furnaces. More accurate full-scale models are still needed for a detailed understanding of the entire process.

CRediT authorship contribution statement

Mads Fromreide: Writing – original draft, Software, Conceptualization. **Dolores Gómez:** Writing – review & editing, Writing – original draft, Supervision, Conceptualization. **Svenn Anton Halvorsen:** Writing – review & editing, Writing – original draft, Supervision, Conceptualization. **Pilar Salgado:** Writing – review & editing, Writing – original draft, Supervision, Conceptualization.

Declaration of competing interest

The authors declare that they have no known competing financial interests or personal relationships that could have appeared to influence the work reported in this paper.

Acknowledgements

This paper is based on the corresponding author's PhD project, which was funded by the project Electrical Conditions and their Process Interactions in High Temperature Metallurgical Reactors (ElMet), with financial support from The Research Council of Norway (Pr.No. 247791) and the companies Elkem and Eramet Norway.

The authors affiliated to CITMAga have also received funding from Xunta de Galicia (Pr.No. GI-1563 ED431C 2021/5) and FEDER, Ministerio de Ciencia e Innovación-AEI research project PID2021-122625OB-I00.

Data availability

No data was used for the research described in the article.

References

[1] S. Olsen, M. Tangstad, T. Lindstad, Production of Manganese Ferroalloys, Tapir Academic Press, 2007.
[2] M. Gasik (Ed.), Handbook of Ferroalloys, Elsevier Ltd., Oxford, 2013.
[3] S. Olsen, M. Tangstad, Silicomanganese production - process understanding, in: INFACON X: Tenth International Ferroalloys Congress, Cape Town, South Africa, 2004, pp. 231–238.
[4] N. Barcza, A. Koursaris, J. See, W. Gericke, The 'Dig Out' of a 75 MVA High-carbon ferromanganese electric smelting furnace, in: 37th Electric Furnace Conference, Detroit, USA, AIME, 1979, pp. 19–33.
[5] E. Ringdalen, M. Ksiazek, Excavation of a SiMn-Furnace, in: J. Steenkamp, A. Cowey (Eds.), Furnace Tapping 2018, S98, Southern African Institute of Mining and Metallurgy (SAIMM), 2018, pp. 167–177.
[6] J. Steenkamp, J. Gous, W. Grote, R. Cromarty, H. Gous, Process zones observed in a 48 MVA submerged Arc furnace producing silicomanganese according to the ore-based process, in: B. Davis, et al. (Eds.), Extraction 2018, in: The Minerals, Metals and Materials Series, Springer International Publishing, 2018, pp. 639–651.
[7] A. Dilawary, J. Szekely, A mathematical model of slag and metal flow in the ESR process, Metall. Mater. Trans. B 8 (1977) 227–236.
[8] M. Dhainaut, Simulation of the electric field in a submerged arc furnace, in: Proceedings of the Tenth International Ferroalloy Congress, 2004, pp. 605–613.
[9] K. Karalis, N. Karkalos, N. Cheimarios, G. Antipas, A. Xenidis, A. Boudouvis, A CFD analysis of slag properties, electrode shape and immersion depth effects on electric submerged arc furnace heating in ferronickel processing, Appl. Math. Model. 40 (21) (2016) 9052–9066.
[10] M. Fromreide, D. Gómez, S.A. Halvorsen, P. Salgado, Induced currents in the lining and steel shell of submerged arc furnaces, J. Sustain. Metall. 9 (1) (2023) 375–385, https://doi.org/10.1007/s40831-022-00625-6.
[11] I. Mc Dougall, Finite element modelling of electric currents in ac submerged arc furnaces, in: R. Das, T.e. Sundaresan (Eds.), Proceedings of the Eleventh International Ferroalloys Congress, New Delhi, India, 18–21 February 2007, 2007, pp. 630–637.
[12] E. Herland, M. Sparta, S. Halvorsen, 3D models of proximity effects in large FeSi and FeMn furnaces, J. S. Afr. Inst. Min. Metall. 118 (6) (2018) 606–618, https://doi.org/10.17159/2411-9717/2018/v118n6a8.
[13] E. Herland, M. Sparta, S. Halvorsen, Skin and proximity effects in electrodes and furnace shells, Metall. Mater. Trans. B (2019) 2884–2897.
[14] Y.A. Tesfahunegn, G. Saevarsdottir, T. Magnusson, M. Tangstad, Comparative study of AC and DC solvers based on current and power distributions in a submerged arc furnace, Metall. Mater. Trans. B 51 (2020) 510–518, https://doi.org/10.1007/s11663-020-01794-z.
[15] A. Bermúdez, M.C. Muñiz, F. Pena, J. Bullón, Numerical computation of the electromagnetic field in the electrodes of a three-phase arc furnace, Int. J. Numer. Methods Eng. 46 (1999) 649–658.
[16] M. Fromreide, D. Gómez, S.A. Halvorsen, E.V. Herland, P. Salgado, Reduced 2D/1D mathematical models for analyzing inductive effects in submerged arc furnaces, Appl. Math. Model. 98 (2021) 59–70, https://doi.org/10.1016/J.APM.2021.04.034.
[17] M. Fromreide, S.A. Halvorsen, M. Sparta, V.K. Risinggård, P. Salgado, D. Gómez, E. Herland, Effects of alternating currents in the hearth of submerged arc furnaces, in: Proceedings of the 16th International Ferro-Alloys Congress (INFACON XVI) 2021, 2021.
[18] J. Acero, C. Carretero, I. Lope, R. Alonso, J.M. Burdío, Analytical solution of the induced currents in multilayer cylindrical conductors under external electromagnetic sources, Appl. Math. Model. 40 (23) (2016) 10667–10678, https://doi.org/10.1016/j.apm.2016.07.031.
[19] K. Kubiczek, M. Kampik, Fast and numerically stable analytical computations for the power induced in cylindrical multilayered conductors under external magnetic fields, IEEE Trans. Electromagn. Compat. 65 (1) (2023) 292–299, https://doi.org/10.1109/TEMC.2022.3217647.
[20] H.-W. Deng, Y.-J. Zhao, C.-J. Liang, W.-S. Jiang, Y. Ning, Effective skin depth for multilayer coated conductor, Prog. Electromagn. Res. M 9 (2009) 1–8.
[21] A. Bermúdez, D. Gómez, P. Salgado, Mathematical Models and Numerical Simulation in Electromagnetism, Springer International Publishing, 2014.
[22] D. Griffiths, Introduction to Electrodynamics, Cambridge University Press, 2008.
[23] AC/DC Module User's Guide, COMSOL Multiphysics® V6.1, COMSOL AB, Stockholm, Sweden, 2022.